15. Özcan, A. S. *et al.* Texture of $TiSi_2$ thin films on Si(001). *J. Appl. Phys.* **92,** 5011–5018 (2002).
16. Tsukada, M. & Ohfuji, S. Structural inheritance from polycrystalline underlayers in the growth of double-layered aluminum films. *J. Vac. Sci. Technol. B* **11,** 326–332 (1993).
17. Tracy, D. P., Knorr, D. B. & Rodbell, K. P. Texture in multilayer metallization structures. *J. Appl. Phys.* **76,** 2671–2680 (1994).
18. Knorr, D. B., Merchant, S. M. & Biberger, M. A. Development of texture in interconnect thin film stacks. *J. Vac. Sci. Technol. B* **16,** 2734–2744 (1998).
19. Joint Committee on Powder Diffraction Standards. *Powder Diffraction File* 38–0844 (International Centre for Diffraction Data, Philadelphia, 1998).
20. Kilaas, R. Optimal and near-optimal filter in high-resolution electron microscopy. *J. Microsc.* **190,** 45–51 (1998).

Supplementary Information accompanies the paper on **www.nature.com/nature**.

Acknowledgements We thank F. M. d'Heurle, J. M. E. Harper, C. Cabral, K. Ludwig, C. Murray, C. Noyan and K. P. Rodbell for discussions, and C. Diareo for TEM sample preparation. C.D. thanks the 'Fonds voor Wetenschappelijk Onderzoek—Vlaanderen' for support. The work at NCEM was supported by the Director, Office of Science, Office of Basic Energy Sciences, Division of Materials Sciences and Engineering, of the US Department of Energy. Pole figures were measured at the NSLS, Brookhaven National Laboratory, which is supported by the US Department of Energy, Division of Materials Sciences and Division of Chemical Sciences.

Competing interests statement The authors declare that they have no competing financial interests.

Correspondence and requests for materials should be addressed to C.D. (christophe.detavernier@ugent.be) or C.L. (clavoie@us.ibm.com).

Coupled spatial variations in precipitation and long-term erosion rates across the Washington Cascades

Peter W. Reiners[1], Todd A. Ehlers[2], Sara G. Mitchell[3] & David R. Montgomery[3]

[1]*Department of Geology and Geophysics, Yale University, 210 Whitney Avenue, New Haven, Connecticut 06511, USA*
[2]*Department of Geological Sciences, University of Michigan, Ann Arbor, Michigan 48109, USA*
[3]*Department of Earth and Space Sciences, University of Washington, Seattle, Washington 98195, USA*

Past studies of tectonically active mountain ranges have suggested strong coupling and feedbacks between climate, tectonics and topography[1–5]. For example, rock uplift generates topographic relief, thereby enhancing precipitation, which focuses erosion and in turn influences rates and spatial patterns of further rock uplift. Although theoretical links between climate, erosion and uplift have received much attention[2,6–10], few studies have shown convincing correlations between observable indices of these processes on mountain-range scales[11,12]. Here we show that strongly varying long-term ($>10^6$–10^7 yr) erosion rates inferred from apatite (U–Th)/He cooling ages across the Cascades mountains of Washington state closely track modern mean annual precipitation rates. Erosion and precipitation rates vary over an order of magnitude across the range with maxima of 0.33 mm yr^{-1} and 3.5 m yr^{-1}, respectively, with both maxima located 50 km west (windward) of the topographic crest of the range. These data demonstrate a strong coupling between precipitation and long-term erosion rates on the mountain-range scale. If the range is currently in topographic steady state, rock uplift on the west flank is three to ten times faster than elsewhere in the range, possibly in response to climatically focused erosion.

The Washington Cascades provide a natural laboratory for observing interactions between climate, tectonics and topography. Although isolated volcanoes in the mountain range are part of an active magmatic arc extending south into California, most of the topographic relief in the Washington Cascades, and essentially all of it north of about 47° N, is the result of deep-seated bedrock uplift and the resultant erosion, rather than volcanic extrusion. Summits in the range seldom reach elevations higher than 2.7 km, but local relief is commonly 1.2–1.8 km. The modern Washington Cascades cast a dramatic orographic rain shadow. Mean annual precipitation rates on the windward west flank are as high as 4 m yr^{-1} and host lush vegetation, in contrast to rates of 0.2 m yr^{-1} or less in the sagebrush steppe directly east of the range. Palaeobotanical evidence[13] indicates that the orographic rain shadow was not as strong before the Late Miocene epoch, so it is likely that at least some of the current topographic expression of the Washington Cascades is younger than 10–15 Myr. This is consistent with the well-known post-15-Myr BP warping and uplift of the lava flows of the east-derived Columbia River basalt group on the eastern side of the range. Little is known about either the kinematics or dynamics of uplift in the Washington Cascades. Global positioning system (GPS) data suggest only weak horizontal crustal shortening across the range[14], and patterns of crustal seismicity and detailed geologic mapping do not suggest any large active Neogene faults or other structures (see the catalogued seismicity record at ⟨http://www.seismo.berkeley.edu/seismo/⟩; also available in the Supplementary Information)[15–19].

We measured bedrock apatite (U–Th)/He ages from samples in a broad (200 km) east–west swath across the Washington Cascades to examine spatial patterns of erosion in a setting with a strong orographic precipitation gradient. The apatite (U–Th)/He system has a closure temperature of ~60–70 °C (ref. 20) and ages generally represent the time since a rock passed through a depth in the crust corresponding to that temperature (typically 1.5–2.5 km), as a result of tectonic or erosional exhumation.

Thirty new apatite He ages from twenty samples from the western flank of the Cascades are shown in Fig. 1, along with our existing data[21] from elsewhere in this swath. Samples were collected from plutons with crystallization ages ranging from ~20–95 Myr BP. In all cases except that of Mt Pilchuck in the far west, apatite He ages are much less than crystallization ages. In this part of the Cascades, plutons younger than ~20 Myr BP are small and rare and there is no evidence in age and pluton distributions that ages reflect a significant component of magmatically controlled heating.

Apatite He ages in this swath of the central Cascades vary from 4.4 to 60 Myr BP (Fig. 1). In single vertical transects collected over short horizontal distances, ages generally show increasing ages, or little change in age, with increasing elevation[21]. The most obvious pattern in the data consists of relatively old ages (>25 Myr BP) at the topographic crest and far eastern and western flanks of the range, and young ages (<12 Myr BP) on the west slope (Figs 1 and 2).

To first order, the ratio of the apatite He closure isotherm depth (~1.5–2.5 km) and age yields an estimate of time-averaged exhumation rate. As there are no known late Tertiary faults or extensional structures in this region[15–19], we assume that this exhumation is entirely erosional. We calculated erosion rates for these samples by relating each apatite He age to cooling-rate-dependent closure temperature and depth through a series of equations with assumed parameters, including geothermal gradient, He diffusion properties[20], thermal diffusivity, and depth to constant temperature[22] (see Supplementary Information). We used sample-specific geothermal gradients based on interpolation of observed gradients ranging from 20 to 40 °C km^{-1} (ref. 23) (Fig. 1). Our model assumes a steady-state distribution of isotherms in the crust, which is fairly robust for the relatively slow erosion rates inferred from these data and tectonic setting over the past 40 Myr (ref. 23).

Closure depth for each sample was adjusted to account for local

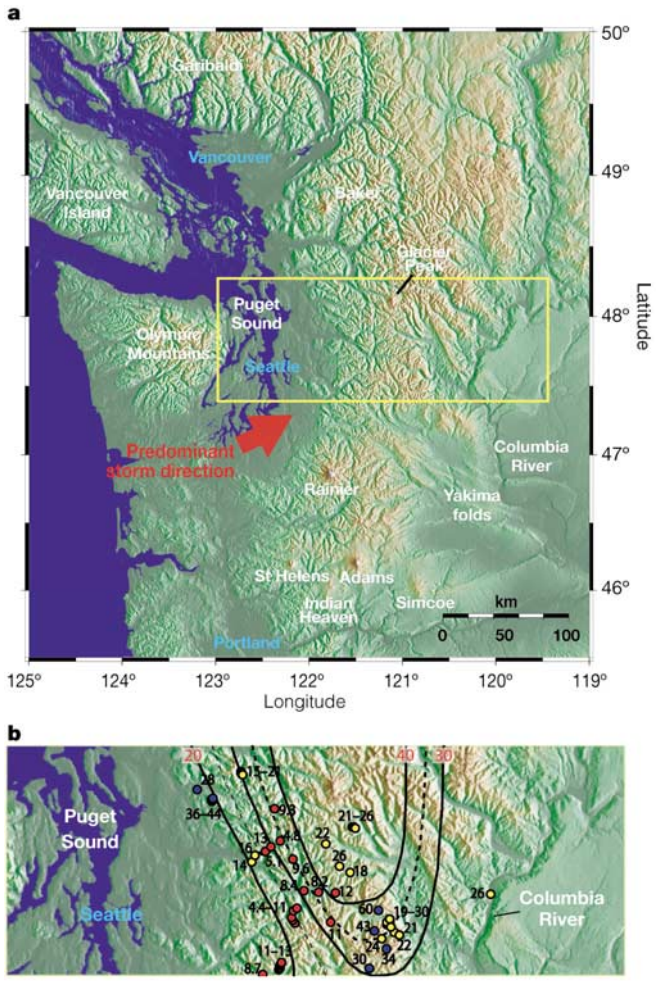

Figure 1 Map of the Washington Cascades and regional features, showing locations of samples and swath for climatic and topographic comparisons. White text, natural features including five active or recently active volcanoes; blue text, cities. Yellow box in **a** indicates location of expanded panel (**b**). **b**, Sample locations and ages (or age ranges, for multiple samples in vertical transects). Sample locations in red denote ages less than 13 Myr BP; yellow, 13–26 Myr BP; blue, >26 Myr BP. Contours of geothermal gradients for 20, 30, and 40 °C km^{-1} from ref. 24 (solid black lines; red text labels) are also shown; intermediate contours (dashed lines) have been interpolated.

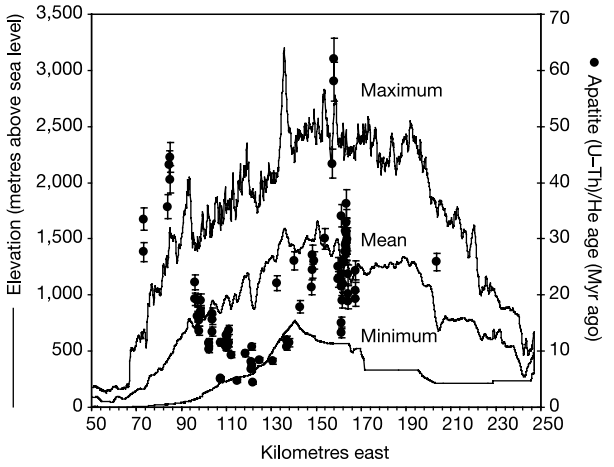

Figure 2 Apatite (U–Th)/He ages and topographic profiles (mean, maximum and minimum elevations) in swath across the Washington Cascades shown in Fig. 1. Ages younger than 10 Myr BP are restricted to the upper western flank of the range. Ages are oldest at the topographic crest or far flanks. Error bars are 6% (2σ), based on reproducibility of standards. The isolated topographic high in the maximum topography profile near 135 km east is Glacier Peak volcano.

topographic effects by adding the difference between sample and mean local elevation (for a 10-km circle) to each closure depth determined by the method above. This effectively assumes constant topography since closure of the apatite He system. Erosion rates calculated in this way represent time-averaged rates since closure. Given the evidence for at least some surface uplift since the Late Miocene, it is therefore possible and even likely that many of these rates, especially those for samples with older ages, have varied. Nevertheless, assuming cooling results primarily from erosional exhumation, our technique captures the average rate at which samples transited the upper crust.

Calculated model erosion rates average 0.10 km Myr^{-1} across the Washington Cascades at this latitude, but vary from as low as 0.02–0.04 km Myr^{-1} on the eastern flank and near the topographic crest, to as high as 0.33 km Myr^{-1} about two-thirds of the way up the west flank (Fig. 3). Calculated erosion rates for samples in some vertical transects display up to 0.08 km Myr^{-1} differences between the highest and lowest elevation samples. This probably reflects faster erosion during the time intervals represented by these ages. This is supported by the slopes of the age–elevation relationships in some vertical transects, suggesting more rapid erosion (up to 0.7 km Myr^{-1}) from ~11–13 Myr BP. Despite these limitations to a steady erosion model, these data provide a useful estimate of long-term erosion rates, and more importantly, their differences across the range. If these rates have persisted since 10–15 Myr BP, approximately 3–5 km of rock have been removed from the mid-slope of the western flank, and only 0.5–1.0 km from other areas, including the topographic crest.

The absence of obvious active structures in the Washington Cascades that could produce spatially variable late Cenozoic rock uplift and erosion rates suggests that some other agent, such as climatic differences across the range, may be responsible for the order-of-magnitude difference in calculated erosion rates. It is reasonable to expect that one of the strongest climatic influences on local erosion rate would be the rate of mean annual precipitation (hereafter referred to simply as precipitation), through its effect on hillslope soil or regolith instability, or fluvial discharge and incision. Precipitation across the Washington Cascades shows a strong orographic effect, due to rising and cooling moist air masses encountering the topographic barrier of the range as they move eastward from the Pacific. Figure 3 shows the precipitation profile across the range centred at the latitude of Seattle, from interpolation of observed precipitation from 1961–1999 (ref. 24). In form and position relative to topography, the precipitation profile across the Cascades is remarkably similar to that of maximum calculated erosion rates (Fig. 3). Mean annual precipitation and calculated erosion reach a maximum of 3.5 m yr^{-1} and 0.33 km Myr^{-1}, respectively, at a mean elevation of about 1.1–1.2 km on the west flank of the range. Elsewhere in the range, including the topographic crest, precipitation is a factor of two to three lower, and calculated erosion rates are about three to fifteen times lower.

Local erosion rate might be expected to depend on several factors in addition to or instead of local precipitation, such as lithology, local slope or fluvial discharge. Bedrock across the entire transect is dominated by granitoid plutonic and gneissic rock, so lithologic variations would be unlikely to cause significant erosion rate variations. Likewise, mean local relief (as a proxy for local slope) in the transect shows little variation (1–1.3 km, for circles 10 km in diameter) across most of the range, and no significant correlation of relief with erosion rate is observed (Fig. 3). Fluvial discharge can be approximated to first order as integrated precipitation upstream,

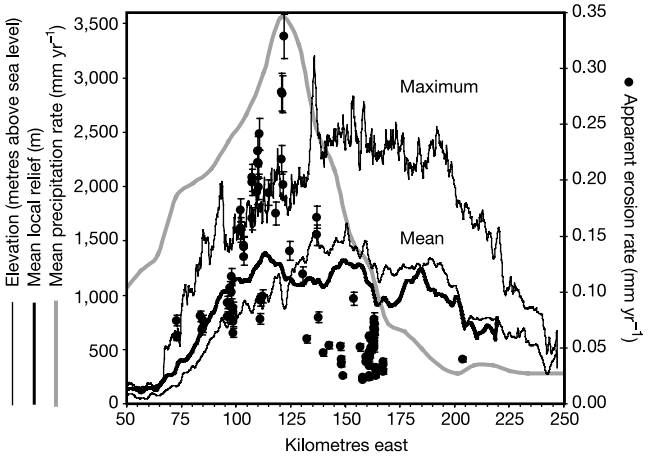

Figure 3 Comparison of topographic profiles, calculated model erosion rates, and mean annual precipitation rates. Thin black solid lines, mean and maximum topographic profiles. Filled symbols, erosion rates calculated from apatite (U–Th)/He ages. Bold grey line, profile of mean annual precipitation rate. Bold black line, mean local relief calculated for circles 10 km in diameter. Calculated erosion rates show a maximum of 0.33 km Myr^{-1} at mean elevations of about 1–1.2 km elevation on the west flank of the range. The mean local relief shows little variation over most of the range, but the mean annual precipitation rate largely follows mean erosion rate, with a maximum of 3.5 m yr^{-1} in the same location as the erosion rate maximum. The precipitation rate maximum at ~120 km east is not an artefact of the orographic effect of Glacier Peak, because the precipitation transect is located near the latitude of Seattle and Mt Stuart, about 50 km to the south.

which is highest in the far western part of the transect, rather than at a mean elevation of ~1 km on the west flank, at the coincidence of erosion rate and precipitation maxima.

No major late Tertiary structures have been identified in the Cascades that could accommodate differential uplift and erosion rates across the range. It is possible that broad arching or folding could lead to higher uplift rates in the core of the range, but by itself (and in a steady state) this would be expected to lead to the highest erosion rates at the topographic crest, rather than 50 km to the windward side, coincident with the highest precipitation. Because of this, we conclude that the long-term erosion rate pattern across the range is controlled primarily by the precipitation pattern. The specific geomorphic processes coupling precipitation and erosion in this case are not clear.

Commonly used stream-power indices predict erosion as a function of main channel slope and discharge, but neither of these parameters correlate with precipitation or erosion rates inferred from apatite He ages. This may suggest a more important role for hill-slope processes or higher-order stream characteristics in controlling variations in long-term erosion rates, because these respond to more local variations in precipitation. Alternatively, variations in extents of glacial erosion across the range may contribute to the spatial pattern of erosion, because ice accumulation would also respond to local variations in precipitation. But, regardless of the specific geomorphic liaison between climate and erosion, these data suggest a predominately climatic influence on spatial variations in erosion rates across the range.

The strong variation in, and correlation between, precipitation and erosion rates across the Washington Cascades supports theoretical studies that argue for strong coupling and feedbacks between climate and tectonics in active orogens[1–10]. Modelling studies suggest that mountain topography evolves towards a steady state, after which the macro-scale topography remains constant and erosion rates are equal to rock uplift rates. It is possible that rock uplift and erosion rates are unrelated, in which case the modern Cascades topography is transient.

However, if the Cascades are in, or even close to, topographic steady state, then rock uplift on the west flank is as much as an order of magnitude faster than elsewhere in the range. The dynamic link by which rock uplift and deformation respond to spatially focused erosion could simply be isostasy, or some other mechanism such as accomodation of pluton emplacement or the vertical component of middle or lower crustal flow into crustal regions experiencing relatively rapid exhumation. In either case, the current orographic climate pattern is well correlated with, and may exert a strong influence on, the distribution of erosion, and possibly rock uplift and deformation, across the Cascades. □

Received 20 June; accepted 2 October 2003; doi:10.1038/nature02111.

1. Beaumont, C., Kooi, H. & Willett, S. in *Geomorphology and Global Tectonics* (ed. Summerfield, M. A.) 29–55 (John Wiley & Sons, Chichester, UK, 2000).
2. Willett, S. D. Orogeny and orography: The effects of erosion on the structure of mountain belts. *J. Geophys. Res.* **104,** 28957–28981 (1999).
3. Zeitler, P. K. *et al.* Erosion, Himalayan geodynamics, and the geomorphology of metamorphism. *GSA Today* **11,** 4–9 (2001).
4. Koons, P. O. The topographic evolution of collisional mountain belts: A numerical look at the southern Alps. *New Zealand. Am. J. Sci.* **289,** 1041–1069 (1989).
5. Montgomery, D. R. & Brandon, M. T. Topographic controls on erosion rates in tectonically active mountain ranges. *Earth Planet. Sci. Lett.* **201,** 481–489 (2002).
6. Beaumont, C., Fulsack, P. & Hamilton, J. in *Thrust Tectonics* (ed. McClay, K. R.) 1–18 (Chapman and Hall, New York, 1991).
7. Willett, S. D., Beaumont, C. & Fullsack, P. Mechanical model for the tectonics of doubly vergent compressional orogens. *Geology* **21,** 371–374 (1993).
8. Willett, S. D., Slingerland, R. & Hovius, N. Uplift, shortening, and steady state topography in active mountain belts. *Am. J. Sci.* **301,** 455–485 (2001).
9. Tucker, G. E. & Slingerland, R. L. Erosional dynamics, flexural isostasy, and long-lived escarpments: A numerical modeling study. *J. Geophys. Res.* **99,** 12229–12243 (1994).
10. Whipple, K. X., Kirby, E. & Brocklehurst, S. H. Geomorphic limits to climate-induced increases in topographic relief. *Nature* **401,** 39–43 (1999).
11. Brozovic, N., Burbank, D. W. & Meigs, A. J. Climatic limits on landscape development in the Northwestern Himalaya. *Science* **276,** 571–574 (1997).
12. Montgomery, D. R., Balco, G. & Willett, S. Climate, tectonics and the morphology of the Andes. *Geology* **29,** 579–582 (2001).
13. Smiley, C. J. The Ellensburg flora of Washington. *Univ. Cal. Publ. Geol. Sci.* **35,** 159–276 (1963).
14. Miller, M. M. *et al.* GPS-determination of along-strike variation in Cascadia margin kinematics: Implications for relative plate motion, subduction zone coupling, and permanent deformation. *Tectonics* **20,** 161–176 (2001).
15. Dragovich, J. D., *et al. Geologic Map of Washington—Northwest Quadrant, Washington* 3 sheets, 1:250,000, 71 pages (Geologic Map GM-50, Washington Division of Geology and Earth Resources, Washington State Department of Natural Resources), (2002).
16. Tabor, R. W. *et al. Geologic Map of the Skykomish River 30- by 60-minute Quadrangle, Washington* 1 sheet, 1:100,000, 42 pages (US Geol. Surv. Misc. Invest. Ser. Map I-1963, 1993).
17. Tabor, R. W., Frizzell, V. A. Jr, Booth, D. B. & Waitt, R. B. *Geologic Map of the Snoqualmie Pass 30 x 60 minute Quadrangle, Washington* 1 sheet, 1:100,000, 57 pages (US Geol. Surv. Misc. Invest. Ser. I-2538, 2000).
18. Tabor, R. W. *et al. Geologic Map of the Chelan 30-minute by 60-minute Quadrangle, Washington* 1 sheet, scale 1:100,000, 29 pages (US Geol. Surv. Misc. Invest. Ser. Map I-1661, 1987).
19. Tabor, R. W. *et al. Geologic Map of the Wenatchee 1:100,000 Quadrangle, Central Washington* 1 sheet, 1:100,000, 26 pages (US Geol. Surv. Misc. Invest. Ser. Map I-1311, 1982).
20. Farley, K. A. Helium diffusion from apatite: General behaviour as illustrated by Durango fluorapatite. *J. Geophys. Res.* **105,** 2903–2914 (2000).
21. Reiners, P. W. *et al.* Late Miocene exhumation and uplift of the Washington Cascades. *Geology* **30,** 767–770 (2002).
22. Brandon, M. T., Roden-Tice, M. K. & Garver, J. I. Late Cenozoic exhumation of the Cascadia accretionary wedge in the Olympic Mountains, northwest Washington State. *Geol. Soc. Am. Bull.* **110,** 985–1009 (1998).
23. Blackwell, D. D., Steele, J. L., Kelley, S. & Korosec, M. A. Heat flow in the state of Washington and thermal conditions in the Cascade range. *J. Geophys. Res.* **95,** 19495–19516 (1990).
24. Daly, C., Neilson, R. P. & Phillips, D. L. A statistical-topographic model for mapping climatological precipitation over mountainous terrain. *J. Appl. Meteorol.* **33,** 140–158 (1994).

Supplementary Information accompanies the paper on **www.nature.com/nature**.

Acknowledgements We acknowledge comments by P. Molnar. We also thank S. Willett and M. Brandon for discussions, and S. Nicolescu for analytical assistance. This work was supported by the US National Science Foundation.

Competing interests statement The authors declare that they have no competing financial interests.

Correspondence and requests for materials should be addressed to P.W.R. (peter.reiners@yale.edu).

Supplementary Information to accompany Reiners, Ehlers, Mitchell, and Montgomery.

Table 1. Single-grain apatite (U-Th)/He data for samples from the west flank of the Washington Cascades.

sample ID	elev. (m.a.s.l.)	corrected age (Ma)	± (2σ) (Ma)	radius (μm)	mass (μg)	U ppm	Th ppm	He (ncc/mg)	Ft	U/Th	model erosion rate (km/myr)	UTM E	UTM N	km E in swath
02CAS10a	634	15.6	0.94	47.5	3.58	16.0	28.5	31.1	0.725	0.56	0.14	608379	5299716	103.7
02CAS10c	634	16.6	1.0	46.1	2.63	23.4	38.9	46.5	0.710	0.60	0.13	608379	5299716	103.7
02CAS11a	250	5.16	0.31	33.8	0.94	4.81	12.8	2.98	0.608	0.38	0.20	612071	5301356	107.4
02CAS11c	250	5.06	0.30	56	4.32	20.1	56.9	15.4	0.751	0.35	0.20	612071	5301356	107.4
02CAS12Aa	329	11.4	0.69	35.3	1.13	23.1	34.9	27.3	0.630	0.66	0.093	615919	5305009	111.3
02CAS12Ab	329	13.8	0.83	30.8	0.80	27.0	48.6	37.4	0.585	0.55	0.076	615919	5305009	111.3
02CAS12Ba	674	9.34	0.56	52.3	3.87	24.4	50.1	30.3	0.741	0.49	0.10	616998	5312166	112.4
02CAS13b	1597	10.8	0.65	73.8	8.32	15.3	9.11	18.4	0.809	1.7	0.20	626262	5272009	121.6
02CAS14a	1466	7.32	0.44	41	2.73	30.3	29.7	22.9	0.695	1.0	0.28	625999	5272302	121.4
02CAS15a	1314	6.84	0.41	43.3	1.72	30.5	21.0	20.2	0.688	1.5	0.28	625627	5272489	121.0
02CAS17a	1079	8.13	0.49	29.5	0.86	26.8	34.4	20.0	0.583	0.78	0.22	625602	5274737	121.0
02CAS18a	725	4.36	0.26	46.5	2.91	67.3	66.4	31.4	0.719	1.0	0.33	626590	5274880	121.9
02CAS19a	421	4.77	0.29	32	1.00	92.6	107.6	41.4	0.608	0.86	0.19	619582	5305719	114.9
02CAS22a	1131	9.55	0.57	51.8	3.30	22.1	16.4	22.2	0.739	1.3	0.17	623062	5289967	118.4
02CAS1b	119	27.6	1.7	62.3	7.10	15.8	25.3	57.1	0.783	0.62	0.074	577709	5328214	73.1
02CAS1c	119	33.5	2.0	35	2.53	22.9	43.3	91.3	0.679	0.53	0.060	577709	5328214	73.1
02CAS2a	1625	44.5	2.7	36.3	0.84	14.1	16.5	59.9	0.619	0.85	0.068	589589	5323438	84.9
02CAS2b	1625	40.5	2.4	33.8	0.91	31.2	18.3	107.7	0.618	1.7	0.075	589589	5323438	84.9
02CAS3a	1436	43.1	2.6	37	0.95	21.9	22.8	89.8	0.631	0.96	0.066	589190	5323652	84.5
02CAS4b	1311	35.7	2.1	40	1.20	24.4	22.2	84.1	0.657	1.1	0.078	588578	5323777	83.9
02CAS5a	1262	22.2	1.3	55.6	3.53	16.3	23.7	43.9	0.747	0.69	0.077	600837	5335209	96.2
02CAS5c	1262	19.3	1.2	35.8	2.36	10.7	23.5	26.6	0.703	0.46	0.090	600837	5335209	96.2
02CAS6b	1137	19.0	1.1	52	6.21	16.0	24.1	37.5	0.755	0.66	0.087	601878	5335067	97.2
02CAS6c	1137	16.1	0.97	40.8	1.89	47.7	63.7	83.1	0.679	0.75	0.10	601878	5335067	97.2
02CAS7a	969	15.4	0.93	52.3	3.95	16.6	20.5	29.9	0.745	0.81	0.10	602544	5334980	97.9
02CAS7b	969	13.6	0.82	53	4.30	35.4	33.2	53.4	0.751	1.1	0.11	602544	5334980	97.9

02CAS8a	820	16.6	0.99	50.5	4.15	29.5	23.3	52.2	0.744	1.3	0.086	603275	5334686	98.6
02CAS8b	820	17.2	1.0	60.8	5.84	24.0	18.0	45.5	0.778	1.3	0.083	603275	5334686	98.6
02CAS9a	622	19.0	1.1	51.3	3.29	27.1	19.3	53.7	0.738	1.4	0.063	603296	5334671	98.7
02CAS9b	622	16.6	1.0	50	4.97	7.53	18.3	17.7	0.740	0.41	0.073	603296	5334671	98.7

Ft is alpha-ejection correction of Farley et al. (2002). Apatite He ages in transect but not reported here are available in Reiners et al. (2002).

Long-term model erosion rates from apatite (U-Th)/He ages

To calculate time-averaged erosion rates from apatite He ages we used the method described in Appendix A of Brandon et al. (1998), modified slightly for the apatite He system. This method assumes a steady-state, one-dimensional section of crust with thermal diffusivity K (here assumed to be 32 km^2/myr) and thickness L (here 40 km), with upper and lower boundaries held at T_S (here 10 °C) and $T_S + g_0 L$, respectively, where g_0 is the geothermal gradient prior to the onset of exhumation. Exhumation (assumed to be erosion) occurs at a constant rate $\dot{e}$, and removal of material from the top is assumed to be balanced by accretion below (e.g., from magmatic accretion or crustal thickening), resulting in constant advection rate towards the surface. Temperature as a function of depth z' and erosion rate $\dot{e}$ for this scenario is described by equation 8 of Stüwe et al., or A2 of Brandon et al.). Temperature of interest is defined to be closure temperature T_c, and the equation is rearranged to yield z' as a function of two unknowns, $\dot{e}$ and T_c, and the previously described parameters.

The second equation is also a function of the unknowns $\dot{e}$ and T_c, and the parameters described above, but T_c is described by the Dodson (1979) equation, in which we use the E_a and D_0 parameters for He diffusion in apatite (Farley, 2000). This second equation describes the cooling rate at closure, which is the product of the exhumation rate and the syn-exhumational geothermal gradient (Brandon et al.'s, A4), which can be derived from the first equation.

The combination of these two equations in $\dot{e}$ and T_c is solved numerically to yield a curve of related model AHe ages, erosion rates, closure depths, closure temperatures, and cooling rates. Finally, because samples were collected at different elevations relative to a mean local elevation, a topographic correction must be applied to

account for the longer exhumation paths of samples collected at high elevation relative to mean local elevation. Thus the difference between sample elevation and mean local elevation is added to Z_c' to determine Z_c. Z_c is then divided by the observed AHe age to yield model erosion rate.

Use of this model assumes that thermal steady-state is achieved rapidly (within 3 myr) after the onset of exhumation, which is robust for the range of ages and model erosion rates inferred from them (maximum of 0.3-0.4 km/myr) in this case. Although g_0 technically represents the geothermal gradient before the onset of exhumation, in this case, the assumed pre-exhumation g, and model-derived syn-exhumation g_0 differ by less than 2 °C for ages older than 15 Ma, and 5 °C for ages between 5-15 Ma. Uncertainty in geothermal gradient in this model causes negligible differences in model erosion rates for most samples, but for very young samples (< 6 Ma), 5 °C/km differences in assumed g_0 can produce maximum differences of 20-28% in model erosion rates. However varying g_0 within 10 °C/km either for all or a subset of specific samples does not shift the position of the peak in model erosion rates.

As described above, this model corrects for topographic effects on bending of closure isotherms to the extent that closure depth is corrected for the difference between sample elevation and mean elevation, as measured by a 10-km diameter circle surrounding the sample location. Thus the effects of isotherm bending by topography with effective wavelengths shorter than 10 km is not considered. The magnitude of error introduced by this can be estimated by considering the maximum effect of short wavelength topography on closure isotherm depths for topography with wavelengths less than 10 km. The maximum topographic relief observed within 10-km circles (λ = 10 km) in this swath is about 1.4 km (maximum topographic amplitude h_0 = 0.7 km). At

λ = 10 km, 60-70 °C isotherms follow topography about 20-30% (α, or admittance ratio is about 0.2-0.3; Reiners et al., 2003). For h_0 of 0.7 km, this is about 140-210 m, or about 9-14% of the closure depth (~1.5 km) for these samples, so the "real" Z_c could be a maximum of 9-14% higher or lower due to short-wavelength (< 10-km) topography. Thus the fact that our model calculation here ignores the influence of short-wavelength topography may introduce errors in the estimated exhumation rates of about 9-14%. Moreover, this is a maximum error, because in general, real 3-D topography will not deflect topography as strongly as predicted by model calculations using 2-D topography.

Map of seismicity in the Washington Cascades and surrounding areas.

Events with coda magnitude (Mc) greater than 2.0, occurring between 1970-2001 are shown. Events with no listed azimuthal gap or fewer than four locating stations are not shown. Data from Berkeley Seismological Lab (http://www.seismo.berkeley.edu/seismo/).

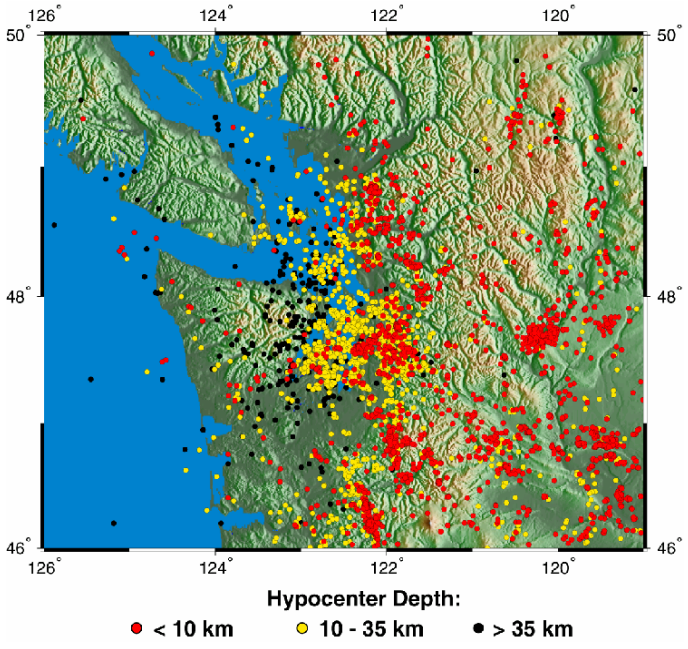

References cited in Supplementary Information and not in manuscript.

Farley, K.A., (U-Th)/He dating: Techniques, calibrations, and applications, *Mineral. Soc. Am., Rev. Mineral. Geochem.* 47, 819-844 (2002).

Stuwe, K., White, L., and Brown, R, The influence of eroding topography on steady-state isotherms. Applications to fission-track analysis, *Earth Planet. Sci. Lett.*, **124**, 63-74.

Dodson, M.E., Theory of cooling ages, in Jaeger, E., and Hunziker, J.C., eds., *Lectures in isotope geology*: Berlin, Springer-Verlag, 194-202 (1979).

Reiners, P.W., Zhou, Z., Ehlers, T.A., Xu, C., Brandon, M.T., Donelick, R.A., and Nicolescu, S., Post-orogenic evolution of the Dabie Shan, eastern China, from (U-Th)/He and fission-track thermochronology, *Am. J. Sci.*, **303**, 489-518 (2003).